Laboratory electron irradiation *Operando* cell for probing synchrotron beam damage mechanisms in lithium-ion battery electrolytes

Yanis Souid, Patrick Soudan, Sylvain Franger, Bernard Lestriez, Nathalie Herlin-Boime, Philippe Poizot, Philippe Moreau, Sophie Le Caër

Laboratory Electron Irradiation *Operando* Cell for Probing Synchrotron Beam Damage Mechanisms in Lithium-Ion Battery Electrolytes

Yanis Souid,[a] Patrick Soudan,[b] Sylvain Franger,[c] Bernard Lestriez,[b] Nathalie Herlin-Boime,[a] Philippe Poizot,[b] Philippe Moreau,[b] Sophie Le Caër[a*]

[a] *NIMBE, UMR 3685, CEA, CNRS, Université Paris-Saclay, CEA Saclay F-91191 Gif-surYvette Cedex, France*

[b] *Nantes Université, CNRS, Institut des Matériaux de Nantes Jean Rouxel, IMN, UMR 6502, 2 rue de la Houssinière, 44000 Nantes, France*

[c] *ICMMO, UMR 8182, CNRS, Université Paris-Saclay, F-91405 Orsay Cedex, France*

**corresponding author: sophie.le-caer@cea.fr*

Abstract

Operando synchrotron techniques provide unique insights into the internal processes of lithium-ion batteries, but radiation-induced effects can alter cell behavior and compromise data interpretation. To better understand these phenomena, we developed an *operando* cell specifically designed for controlled irradiation studies, replicating synchrotron-like conditions, but at the laboratory scale. The electrolyte was selectively irradiated with an electron beam at doses of 5 and 10 kGy, and the resulting impacts on electrochemical performance of a silicon-based electrode, gas evolution, and solid electrolyte interphase (SEI) composition were investigated. Irradiation led to immediate and dose-dependent degradation of cycling performance, with the 10 kGy-irradiated cells failing within four cycles. Gas analysis revealed increased formation of H_2, CO_2, CO, and CH_4, the latter two gases being not produced in the non-irradiated cells, as well as the generation of specific compounds such as C_2H_6 and CH_3CHO, absent in non-irradiated cells. While most gases showed dose-dependent production, H_2 remained relatively insensitive to irradiation levels, likely due to residual water content. After irradiation followed by cycling of the cell, microscopic and electrochemical impedance spectroscopy analyses indicated significant modifications of the electrode surface and SEI morphology, with the formation of porous or inhomogeneous layers that promote further electrolyte degradation and gas release. These findings underscore the importance of accounting for beam-induced effects in *operando* studies with a focus on the

effect of the irradiation of the electrolyte and provide a framework for understanding radiation-accelerated ageing mechanisms in lithium-ion batteries.

Introduction

Li-ion batteries have emerged as a cornerstone technology for modern energy storage applications, from portable electronics to electric vehicles and renewable energy systems. Their widespread adoption is driven by their high energy density, long cycle life, and relatively low self-discharge rates. However, the complexity of the electrochemical and structural transformations occurring within Li-ion batteries during operation presents significant challenges to understanding and improving their performance, safety, and longevity. *Operando* studies, which allow the simultaneous measurement of dynamic processes under realistic operating conditions, have emerged as a powerful approach to probe the internal mechanisms of Li-ion batteries in real time.[1-4] This approach provides invaluable insights into dynamic phenomena such as phase transitions, ion diffusion, and the formation of the solid-electrolyte interphase (SEI) at the surface of electrodes, all of which are critical to the performance and longevity of batteries.

Synchrotron facilities, with their high-brilliance X-ray sources, have significantly advanced *operando* studies by offering exceptional spatial and temporal resolution.[5-7] However, the intense photon flux inherent to synchrotron radiation can induce irradiation/radiation chemistry effects known as “beam damage”, potentially altering the very processes under investigation.[8-10] This damage manifests through mechanisms such as radiolysis of the electrolyte,[11-12] morphological change[13] and structural modification of electrode materials, leading to skewed data and misinterpretation of battery behavior.[14-15] Using *operando* X-ray diffraction measurements, Black *et al.* have shown that radiation effects in *operando* experiments arise mainly from photoionization and the cascade of secondary electrons reaching the particle-electrolyte interface.[15] The authors have shown that these mechanisms explain discrepancies in reported dose estimates and highlight that the electrolyte itself can be altered under irradiation and that overall, beam effects result from coupled radiation and material factors, making them difficult to predict.[15] Studies have demonstrated that beam damage is influenced by both the dose and dose rate of X-ray exposure, potentially triggering artificial phase transitions[14] and other unintended modifications in battery components, thus necessitating careful consideration in experimental design.[9, 14-16] Moreover, since next-

generation synchrotron sources, such as fourth-generation light sources, offer unprecedented brightness and coherence, the potential for beam-induced effects becomes even more pronounced. These advanced facilities can for instance lead to significant beam heating effects, with temperature increases exceeding 400 K in certain materials.[17] All these works highlight the importance of accounting for synchrotron-induced effects when designing and interpreting *operando* experiments on lithium-ion batteries.

However, only a limited number of studies have examined the impact of X-ray beams on battery materials, and most have concentrated on the electrodes while largely neglecting the electrolyte.[9-10, 13-15] This oversight is significant because changes in the electrolyte can for instance alter the solid electrolyte interphase (SEI), ultimately affecting the performance of the entire battery assembly. To address these challenges, it is essential to investigate radiation-induced processes through controlled radiation chemistry experiments before undertaking synchrotron-based studies. In this regard, preliminary "lighter" pre-synchrotron experiments that employ radiation chemistry techniques are invaluable. Indeed, by simulating the effects of ionizing radiation on battery components, it is possible to anticipate potential beam-induced alterations and develop strategies to minimize them.

To date, no *operando* cell has been developed that enables a comprehensive investigation of battery function by simultaneously assessing the role of the electrolyte and conducting radiation chemistry experiments to simulate synchrotron-induced damage. Such a cell would provide precious insights into the effects of accelerated ageing in these systems.[12, 18-19]. The objective of this work is to fill in this gap by introducing a cell that not only supports battery cycling,[20] but also enables quantification and identification of gases evolved -both under irradiation and in its absence- and facilitates *post-mortem* electrode analysis. This setup replicates synchrotron experimental conditions while serving as a platform to study intrinsic ageing mechanisms accelerated by radiation.[11-12, 18-19, 21-22] Building on this approach, we use a 10 MeV electron accelerator as a complementary and experimentally flexible irradiation source, allowing us to reproduce key features of synchrotron exposure under milder and more controlled conditions, and to directly compare the effects induced by both types of ionizing radiation. Although synchrotron X-rays and high-energy electrons interact with matter through different primary mechanisms, both ultimately generate ionization and excitation leading to similar radiolytic pathways.[23] Hard X-rays deposit energy via photoelectric absorption and Compton scattering, producing high-energy photoelectrons and diffuse

secondary-electron cascades.[24] In contrast, 10 MeV electrons lose energy through inelastic collisions along tracks, generating more clustered ionizations.[23] Their penetration depths differ markedly (~4–5 cm for 10 MeV electrons in low-Z materials versus several millimetres to centimetres for hard X-rays[25]), leading to distinct dose profiles. Beam-induced heating is also source-dependent: focused synchrotron beams can produce significant local heating, while pulsed electron beams may induce transient thermal spikes but their energy deposition profile and charge nature may moderate continuous heating. Despite these differences, the downstream radiation chemistry driven by secondary electrons remains fundamentally similar, enabling a meaningful comparison of beam-damage phenomena. Using a high-energy electron accelerator also offers a broader relevance beyond synchrotron-based studies. Similar irradiation-induced artefacts may arise in *operando* TEM experiments employing liquid electrochemical holders, where the electrolyte is exposed to intense electron beams. Lastly, before attempting to interpret the properties of the SEI in such configurations, it is essential to verify that the electrolyte itself does not generate beam-induced species that could subsequently alter the SEI chemistry or morphology. Establishing this baseline is crucial for disentangling intrinsic electrochemical processes from artefacts introduced by the probing technique.

Silicon was chosen as the active material for the working electrode, primarily because its pronounced SEI formation facilitated experimental observation,[26] and secondly because its well-documented behavior in the literature enables meaningful comparison.[27] Indeed, the SEI is particularly sensitive to beam-induced effects, and any modification of its structure or chemistry can directly influence lithium transport and interfacial kinetics.We demonstrate that, despite the challenging electrode composition, the optimized *operando* cell supports extended cycling while enabling both quantitative gas measurements and Electrochemical Impedance Spectroscopy (EIS). Furthermore, when complemented with advanced spectroscopies, the setup reveals that electrolyte irradiation at doses relevant to synchrotron X-ray experiments induces a sudden and profound alteration of the SEI, even when the irradiation occurs away from the electrode surface, i.e., far from the SEI formation site. Due to the particular sensitivity of silicon electrodes, one cannot infer a symmetric influence on the formation of the cathode-electrolyte interphase (CEI) at the positive electrode. As a result, the present study does not aim at directly reproducing typical *operando* synchrotron conditions nor at providing a quantitative comparison with Ni-rich cathode materials such as

NMC811. Nevertheless, we demonstrate that the electrochemical response of a full system cannot neglect the behaviour of the negative electrode, even when it is not directly irradiated.

Materials and Methods section

Silicon electrode preparation

Nanometric silicon (particles size 150 nm, specific surface area 13.8 $m^2 \cdot g^{-1}$) was used as an active material. Ultrathin platelets of graphite consisting of short stacks of graphene sheets (xGnP graphene nanoplatelets grade M, thickness ~ 6-8 nm, Da_{vg} = 15 μm, specific surface area 120 to 150 $m^2 \cdot g^{-1}$ XG Sciences) was used as conductive additive. Tannic acid (TA, Mw = 1700, Sigma-Aldrich) was used as binder.[28] The water used was ultrapure (<0.05 $\mu S \cdot cm^{-1}$). Slurries were prepared from a mixture of silicon, TA binder and conductive additive. The solid loading in the slurry was 22 wt%. The mixing was performed at 500 rpm for 1 h using a Fritsch Pulverisette 7 mixer with 3 silicon nitride balls (9.5 mm diameter). The slurries were tape cast onto a 28 μm thick copper foil (99.99%, MTI) by using an automatically moved Doctor blade (150 μm blade gap, speed 5 $mm \cdot s^{-1}$). The electrode film was firstly dried at room temperature overnight before being punched out into disks of 10 mm diameter. Finally, the obtained electrodes discs were dried at 100 °C under vacuum for 2 h to remove the residual water. The Si mass loading was between 1.5 to 2 $mg \cdot cm^{-2}$. Electrode fabrication conducted to an overall porosity of around 45%.

Swagelok cells

For comparison purpose, Swagelok-type electrochemical cells were used with the same silicon electrodes as for those for the *operando* cells in "half-cell" configuration (with lithium metal as the negative electrode). Two borosilicate glass-fiber (Whatman GF/D) and one polypropylene (PP) membrane (2500 grade, diam. = 13 mm, thickness 25 μm; Celgard) were used as separator and were soaked in 300 μL of electrolyte consisting of LP30: 1 M $LiPF_6$ solution in EC-DMC (1:1) + 10 wt% FEC. This electrolyte formulation is considered as well suited for silicon-based electrode formation of a SEI[29-30] and was also used in the *operando* cell evaluation.

Galvanostatic cycling was performed using a SP-150 galvanostat-potentiostat (BioLogic S.A., Seyssinet-Pariset, France). Cells were cycled between 0.05 and 1 V vs. Li^+ /Li. The cycling

rates were set to C/40 for the first cycle, C/20 for the following three cycles, and C/10 for the subsequent cycles (considering a specific capacity of 3579 $mAh.g_{Si}^{-1}$).

Electrochemical impedance spectroscopy experiments

Electrochemical impedance spectroscopy (EIS) measurements were performed at room temperature using a VMP3 electrochemical workstation (BioLogic S.A.). The frequency range spanned from 184 kHz to 100 mHz, with a sinusoidal excitation voltage of 10 mV. The system was considered to have reached equilibrium when the open-circuit potential drifted by less than 0.1 mV over a period of 1 hour.

Impedance spectra were analyzed using Zplot software (Scribner Associates). A fit was considered acceptable when the quality factor χ^2 was below 10^{-3} and the relative error for each fitted electrical equivalent circuit (EEC) parameter was less than 5%. High- and mid-frequency regions show semicircles associated with interfacial processes like SEI layer formation, and charge transfer resistance/double layer capacitance. The low-frequency region reveals ion diffusion processes within the electrode or blocking layers. To analyze these contributions, spectra are fitted using an equivalent electrical circuit (EEC) that includes: i) R_0: electrolyte resistance; ii) R_{CT}: charge transfer resistance; iii) C_{dl}: double layer capacitance; iv) R_{SEI} and C_{SEI}: SEI resistance and capacitance, modeled via a constant phase element (CPE) to account for non-ideal capacitive behavior and v) W porosity governed diffusion impedance, modeled with a modified Warburg-Transmission Line Model (TLM) element in order to take into account the noticeable tortuosity throughout the composite electrode vicinity. This EEC modeling allows separation and quantification of redox kinetics, interface properties, and ion transport processes. For more explanations on EEC and their modeling, please refer to reference [19].

Gas measurements produced upon cycling or irradiation

Gases produced during cycling or irradiation were quantified using micro-gas chromatography (μ-GC) to detect H_2, O_2, N_2, CH_4, CO, and CO_2 (when present), and additional gaseous products were identified by gas chromatography coupled to mass spectrometry (GC-MS).

The µ-GC analysis was performed on a µ-GC-R3000 SRA instrument with ultra-pure argon and helium as carrier gases. The detection limits were 2 ppm for H_2 and CO_2, 10 ppm for CH_4 , and 25 ppm for CO, O_2, and N_2. Prior to cycling or irradiation, the *operando* cell atmosphere was repeatedly purged and replenished with ultra-pure argon (1.6 bar, 99.9999%) to ensure an air-free environment. It is noteworthy that the electrolyte was stored in a glovebox under argon and was bubbled with argon for 30 minutes before use.

Subsequently, the production of other gases was identified using a GC-MS system (Agilent Technologies 6890 GC coupled with a 5977 MS) with helium as the carrier gas at a flow rate of 2 $mL \cdot min^{-1}$. The injector operated in splitless mode at 110 °C, and gas separation was achieved using a Varian CP-PorabondQ column (25 m length, 0.32 mm inner diameter). The instrument was purged and cleaned with ultra-pure argon between each measurement.

Irradiation

To irradiate the electrolyte (only) in the *operando* cell, pulse electron irradiation from the ALIENOR linear accelerator was employed. Electrons with an energy of 10 MeV were delivered in 10 ns pulses at a frequency of 2 Hz, effectively minimizing sample heating. Dosimetry was carried out using a Fricke dosimeter (see the Results section for further details).

In recent years, several studies have examined beam damage phenomena during *operando* synchrotron experiments on batteries.[9, 14-15, 31] Although these investigations primarily focus on electrode behavior, they also report estimated irradiation doses absorbed by the electrolyte. For instance, Blondeau *et al.* estimate that, in *operando* synchrotron X-ray absorption spectroscopy experiments, the electrolyte in their THF-based cell typically receives around 18 kGy (1 Gy = 1 $J.kg^{-1}$) over a 5- minute acquisition, for which the associated macroscopic temperature rise is minimal in this case, meaning that only irradiation-induced damage is expected to be significant.[9] In *operando* X- ray diffraction experiments, Jousseaume *et al.* report that the electrolyte absorbs a dose ranging from a few kGy to several tens or even hundreds of kGy.[14] While these works concentrate mainly on electrode effects, it is equally critical to focus on the electrolyte and to better understand how it degrades when subjected to doses on the order of a few kGy (up to 10 kGy). Gaining this insight is essential for designing *operando* synchrotron battery experiments under optimal conditions. In the present work, we thus decided to work with doses of 5 and 10 kGy.

STEM-EELS experiments

Silicon electrodes were recovered after cycling, lightly washed with a few drops of dimethylcarbonate (DMC) and dried in a glove box under argon. Electrodes were scratched and deposited on a holey-carbon cupper grid and transferred in the transmission electron microscope (TEM) with a vacuum transfer sample holder Gatan 648. The details of the EELS phase mapping method based on Multiple Linear Least Squared (MLLS) fitting of the low energy-loss part of the spectrum can be found in reference.[32] Experimental parameters (Themis Z microscope settings, processing method…) are identical to those used for analyzing silicon/graphite anodes in an ethylene carbonate (EC)-free electrolyte.[33]

Results and Discussion

Operando electrochemical cell for cycling, gas analysis and irradiation

Experimental cell architecture and features

The experimental glass cell is composed of two detachable parts that are joined using a Rotulex-type airtight junction system (spherical joint, size 29/15) with a Viton O-ring (see Figure 1a). The upper section features two tungsten wires that pass through and are welded into the glass, ensuring a perfect seal, while serving as the electrochemical connections. In the lower section, these tungsten wires extend into current collectors via screw terminals that are safeguarded against corrosion by an epoxy resin coating (Torr Seal vacuum epoxy) (Figure 1).

The working electrode current collector is a stainless-steel sheet (0.25 mm thick) precisely cut to match the cell's geometry, supporting a maximum square electrode of 1 cm × 1 cm. In contrast, the counter/reference electrode current collector is formed directly by the electrode itself, which is a composite mixture of $FePO_4$-$LiFePO_4$ (FP-LFP) pressed into a stainless-steel grid (AISI 316). To ensure optimal electrical contact between the electrodes and their current collectors, two neodymium magnets, embedded in Torr Seal® low-vapor-pressure epoxy, were placed on opposite sides of the assembly (Figures 1c-1d). The choice of the FP-LFP counter electrode in the *operando* cell avoids gas evolution and volume changes associated with Li, which could obscure the silicon electrode behaviour and impair cycling stability.

Moreover, FP-LFP and Si electrodes can be assembled in air, greatly simplifying cell preparation for the constrained geometry of the *operando* glass setup.

The FP-LFP counter/reference electrode, chosen for its high cycling stability, was designed with a considerable excess capacity relative to the working electrode (approximately 10 mAh compared to 5 mAh). The FP-LFP composite was prepared by mixing the appropriate proportions of FP and LFP in a mortar with 20 wt% carbon (Super P Timcal) and 5 wt% PTFE (Sigma Aldrich). FP was obtained from LFP (provided by Blue Solutions company) by chemical delithiation in slightly over-stoichiometric amount of $NOBF_4$ dissolved in acetonitrile. The resulting composite film was then pressed into a stainless-steel grid at 5 $t \cdot cm^{-2}$ to form the electrode. The mass of active material was ~1.5 mg for the silicon electrode and ~100 mg for the FP-LFP composite electrode.

All electrodes (silicon and LFP), along with the separator and neodymium magnets, were dried at 90 °C overnight under vacuum in a glass oven (Büchi B-585 Drying). The components of the *operando* cell were first cleaned with ethanol and then dried overnight in a vacuum oven at 105°C. The cell was then assembled in an argon-filled glovebox, with the electrodes separated by glass microfiber filter (Whatman GF/D), and the entire assembly was directly immersed in the electrolyte (5 mL, see the justification below). For the negative silicon electrode, fluoroethylene carbonate (FEC) is the primary electrolyte additive, as it facilitates the formation of a stable solid electrolyte interphase (SEI), enhancing mechanical stability.[29-30] Additionally, FEC reduces polarization and overall system impedance, thereby improving cycling stability. As a result, the chosen electrolyte was a 1:1 (v/v) mixture of ethylene carbonate (EC) and dimethyl carbonate (DMC) with 1 M $LiPF_6$, supplemented with 10% FEC (LP30 + 10% FEC).

The cell is sealed with a metal valve that permits gas analysis using micro-chromatography (μ-GC) or gas chromatography coupled to mass spectrometry (GC-MS) (Figure 1d). Additionally, the cell can be exposed to ionizing radiation; in the configuration we used, only the electrolyte is irradiated while the electrodes remain shielded (see Figure S1). This choice allows us to irradiate specifically the electrolyte only. Because 10 MeV electrons are highly penetrating and the beam size is on the order of a few cm^2, the cell geometry must ensure that only the liquid phase lies within the irradiation path. Consequently, a relatively large electrolyte volume (5 mL) is required so that the reactive species generated in the irradiated zone can subsequently reach the electrode surfaces by diffusion or convection.

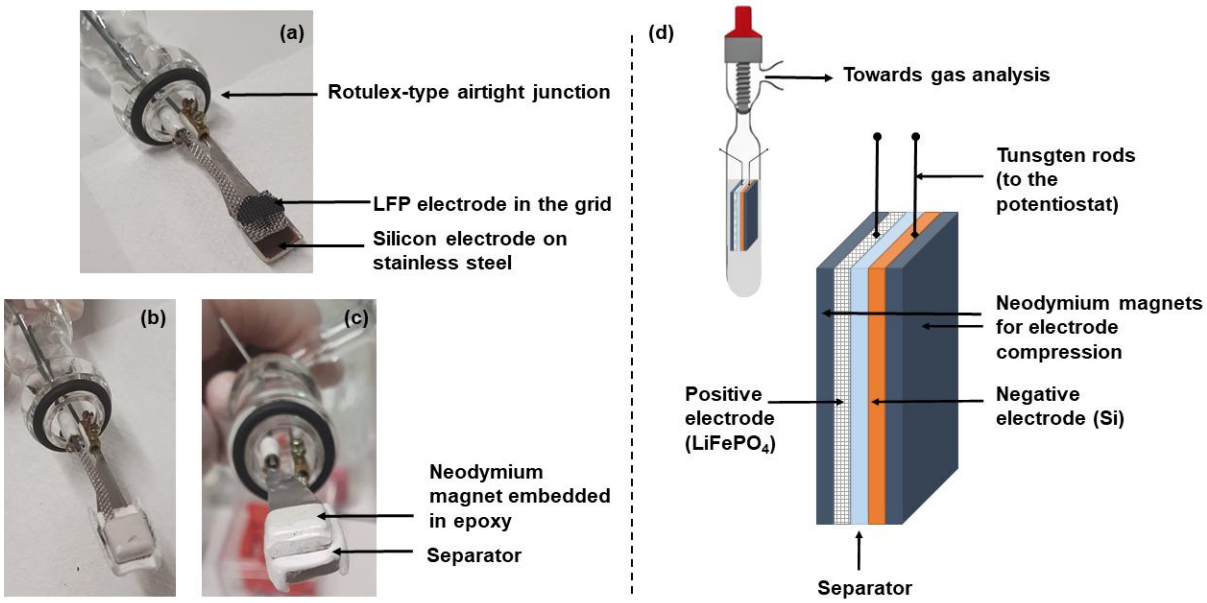

Figure 1. *(a, b, and c) Photographs of the lower part of the cell, which allows for cycling, gas measurements, and irradiation experiments. (d) Schematic representation of the separator, the two electrodes, the magnets, and the connection to the potentiostat via tungsten wires. A diagram of the cell is shown above. In this diagram, the Rotulex junction in the lower part is not depicted. The electrolyte is represented in gray. The metal valve at the top enables the analysis of gases produced within the cell.*

Cell cycling and comparison with a Swagelok-type electrochemical cell

The *operando* cell was cycled over a potential range from –2.40 to –3.40 V vs. FP/LFP corresponding to 1.05 to 0.05 V vs. Li^+/Li, respectively. The cycling range was thus equivalent to that used for the Swagelok cells. It should be reminded that Swagelok cells utilized only 300 µL of electrolyte, in contrast to the *operando* cell where around 5 mL are used.

For both cell types, the following charge regimes were applied: *i*) C/40 (with complete lithiation and delithiation lasting 40 hours each) to promote the formation of a stable, high-quality solid electrolyte interphase (SEI); *ii*) next three cycles at C/20 and *iii*) subsequent cycles at C/10. Figure 2 displays the cycling results. They reveal a significant polarization of 350 mV in the *operando* cell (Figure 2a), while the polarization in the Swagelok cell is slightly lower at 290 mV (Figure 2c). This polarization is measured after the first cycle as the difference of potential at half-charge and half-discharge. First lithiation capacities are quite

similar for both cells: 3357 mAh·g^{-1} for the *operando* cell (Figure 2b) and 3595 mAh·g^{-1} for the Swagelok cell (Figure 2d), showing that the electrochemical process in the *operando* cell is quite representative to that found in a Swagelok cell. However, as presented in Figure S2, the capacity fade after 20 cycles is stronger in the *operando* cell and can even lead to its premature end-of-life. Several factors may explain this deterioration: *i*) despite the pressure exerted by the strong magnets, the successive large volumetric expansion/contraction of silicon might affect more the *operando* cell electrode; *ii*) the higher polarization observed in the *operando* cell might lead to faster reach of the lower potential limit, accelerating the degradation of the cell performance; *iii*) it is also very likely that after over a week of cycling (> 20 cycles), the airtightness of the *operando* cell might be compromised, leading to water ingress that accelerates performance decline; *iv*) the larger amount of electrolyte in the *operando* cell compared to the Swagelok cell is also a well-known factor to be detrimental to cycling performance. Nevertheless, as explained previously, performance of both cells up to the 10th cycle are quite similar and as will be seen later, a dramatic influence of irradiation can be observed within the first few cycles. Consequently, our *operando* cell design is quite relevant to test how irradiation influences the critical initial formation of the SEI.

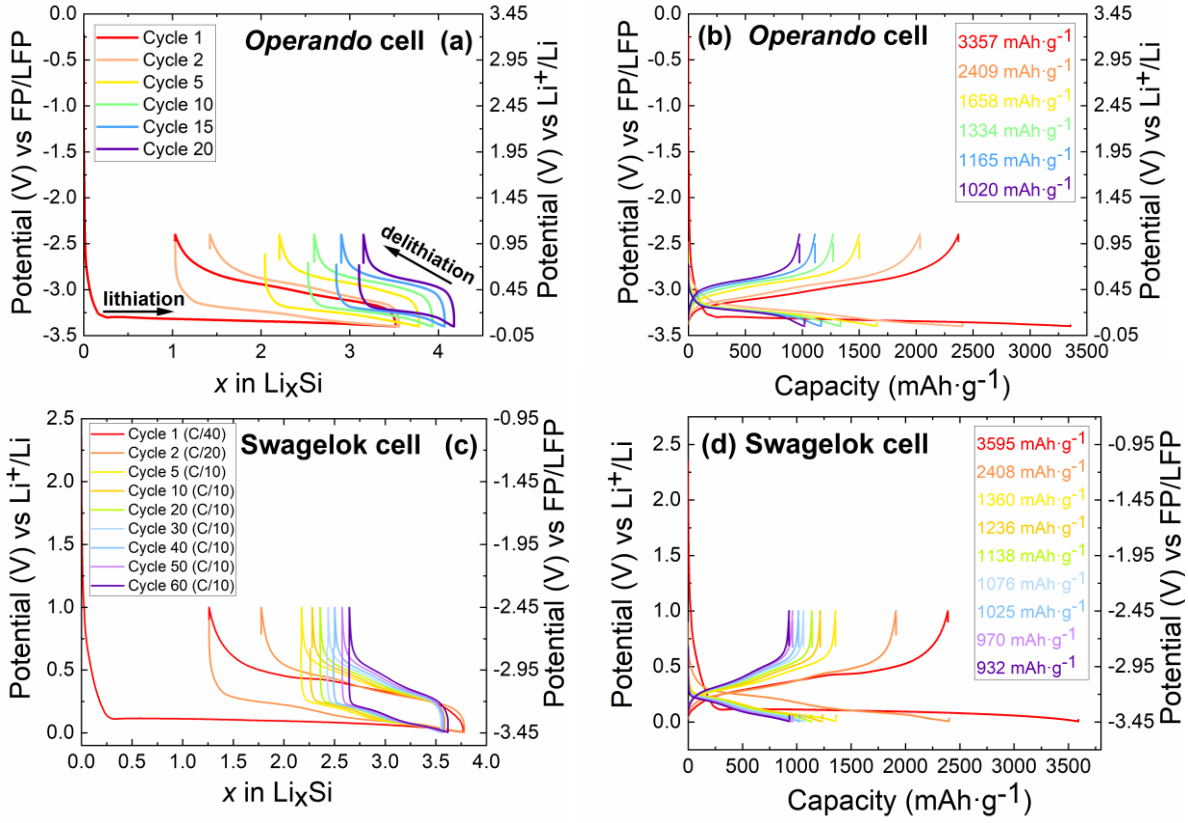

Figure 2. *Comparison of typical potential-composition curves for silicon-based electrodes using the operando cell (a) and the Swagelok cell (c). Corresponding potential-specific capacity profiles are shown in (b) and (d), respectively. The same color code is used for (a) and (b), as well as for (c) and (d).*

Gas production in the operando cell without irradiation

We observed that fluctuations in internal pressure during gas release in the micro-chromatography measurements significantly reduced the *operando* cell's cycling performance compared to experiments without this measurement. Consequently, µ-GC experiments were conducted exclusively during the first cycle. Conversely, GC-MS analyses were performed after the cell had completed 20 cycles.

Detailed study of the first cycle

Gas production during the first lithiation and delithiation were compared at a rate of C/40. Gas quantities were measured at regular intervals except during the night. It is well established in the literature that a low rate in reduction (typically at C/40) in the first cycle facilitates the formation of a stable solid electrolyte interphase (SEI) and is generally accompanied by significant gas evolution.[34] In the present case, only H_2 and CO_2 were detected by µ-GC under our experimental conditions. For example, neither CO nor CH_4 were observed. The H_2 and CO_2 gas production results are presented in Figure 3 in cumulative form. Note that very similar H_2 and CO_2 amounts were obtained at a C/20 rate (data not shown). H_2 production increases linearly with cycling time (Figure 3a).

During cycling, gases are produced exclusively at the silicon electrode (see Photo S1). As expected, the use of a FP/LFP electrode prevents the electrolyte from decomposing at the counter-electrode, so gas formation is restricted to the silicon side. Notably, H_2 and CO_2 are generated during cycling, with CO_2 being produced at a level roughly 10 times lower than that of H_2 (Figure 3). This higher ratio of hydrogen to carbon dioxide aligns with other literature reports.[30, 35] These gases are commonly detected in cells containing a silicon electrode.[30, 35-36] CO_2 is mostly generated by the reduction of FEC and is accompanied by the formation of solid decomposition products (such as LiF) that contribute to the formation of the solid electrolyte interphase (SEI).[36] This reduction reaction also produces some H_2.[36] CO_2 formation occurs during both lithiation and delithiation (see Figure 3b), with higher amounts

observed during lithiation. Consequently, the SEI is also formed -albeit to a lesser extent- during delithiation, as previously reported in reference [30]. This observation likely explains the beneficial effect of FEC on the silicon electrode, as the formation of LiF, which accompanies CO_2 production, [29, 36] helps limiting cracking, particularly during delithiation. In contrast, H_2 production likely originates from trace amounts of water present in various cell components.[36-37] It is also generated during SEI formation.[36] It remains nearly constant, evolving linearly with cycling time, with slightly lower values in delithiation. (Figures 3a-3b). The presence of H_2 during delithiation raises questions about its origin. Since the experiments are carried out over long periods, it is likely that small leaks allow traces of water to enter the cell, thereby leading to the formation of H_2. Globally, as far as H_2 and CO_2 production are concerned, the *operando* cell behaves thus similarly to what has been observed in literature for such kind of electrodes.

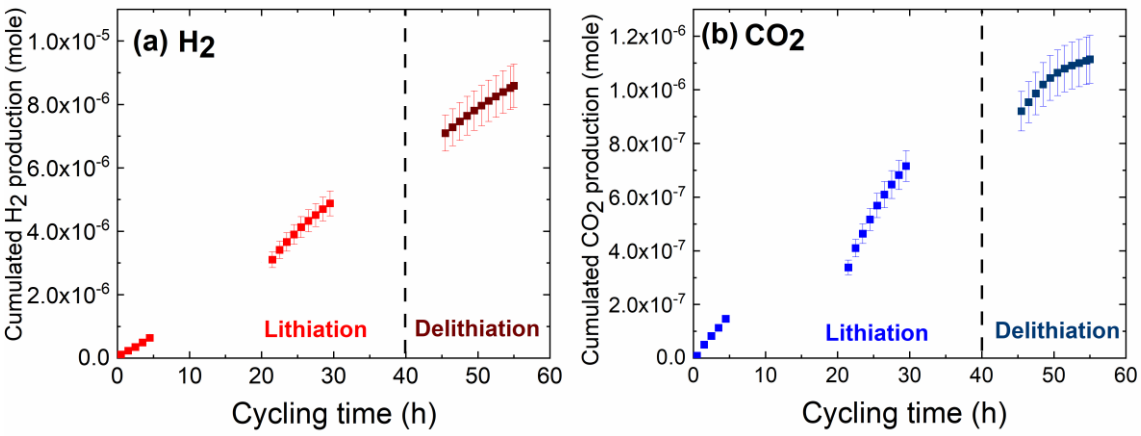

Figure 3. *Cumulative production of H_2 (a) and CO_2 (b) during operando cell cycling. Red and blue squares represent cycling at a C/40 charge rate. The dotted line marks the transition from lithiation to delithiation.*

Gas production analyzed by GC-MS

Additional GC-MS analyses were carried out after complete cycling of the cell (one cycle at C/40, three cycles at C/20, and sixteen cycles at C/10) to accumulate a sufficient amount of gas for accurate analysis. The chromatogram is shown in Figure S3. After cycling the *operando* cell, several gases were detected, including CO_2, C_2H_4,[38] CH_3OH, C_3H_6 and $(CH_3)_2O$. Similar compounds were observed by Gachot *et al.* during the cycling of a cell containing the same electrolyte without any additives.[39] Their work also detailed the influence

of each electrolyte component on gas formation, concluding that C_2H_4 predominantly originates from the reduction of the cyclic carbonate (EC), while CH_3OH and $(CH_3)_2O$ result from the reduction of the linear carbonate (DMC). We can also assume that C_3H_6 originates from the reduction of the linear carbonate. CO_2 formation was attributed to both solvents.[39] Consequently, apart from a peak attributed to $Si(CH_3)_2F_2$ because of a reaction of the electrolyte with the glass tube of the *operando* cell, the nature of the gases is similar to those obtained in typical electrodes in coin cells.[39]

Characterization of the surface of the Si electrode after cycling

STEM-EELS measurements were performed after one cycle at C/40 inside the *operando* cell, at the end of delithiation. In Figure 4 are presented phase maps extracted from STEM-EELS measurements as developed by Xiong et al.[33] These maps for non-irradiated samples resemble closely those typically observed in silicon-based electrodes.[33] As illustrated in Figure 4, the silicon morphology begins to undergo pulverization, with silicon filaments emerging within a polymeric phase characteristic of the organic component of the SEI and of the binder. LiF patches and layers (in green) appear to be randomly distributed around the silicon. Notably, polymer accumulation is especially pronounced around the graphene additive (Figure 4c). These images are strikingly similar to those obtained after 30 cycles in reference [33] although in our study the binder is tannic acid instead of PAALi binder (with PAA representing polyacrylic acid). These results provide further confirmation of the conclusions drawn from the work of Kana *et al.*[28], which showed that tannic acid forms a polymeric compound during the first cycle, likely adsorbed on the surface of silicon particles.

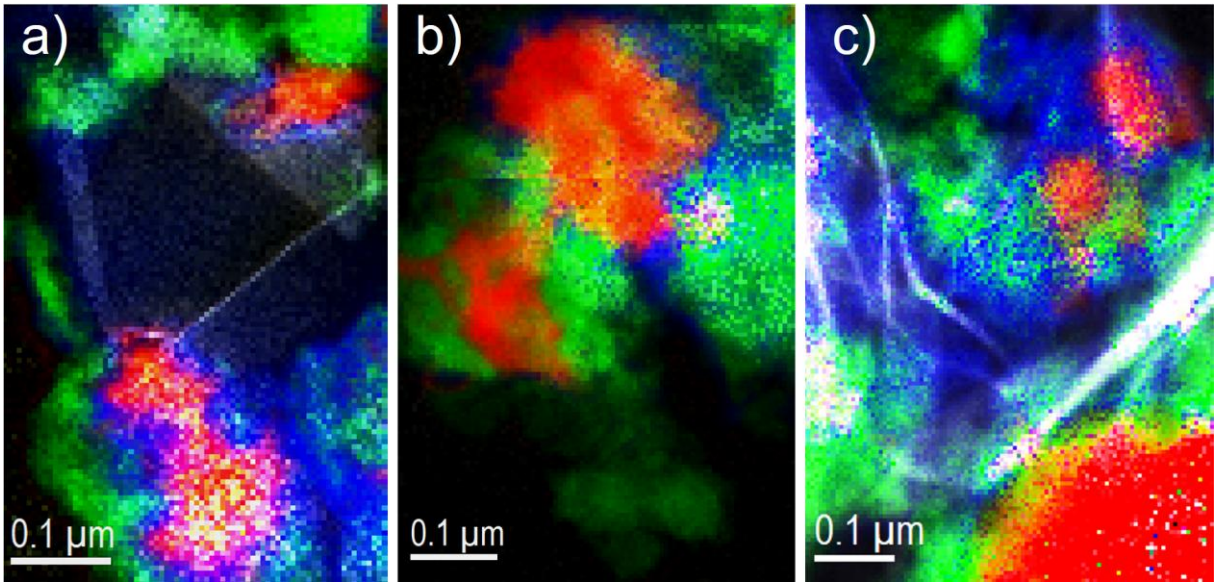

Figure 4. *Phase maps obtained from STEM-EELS experiments on an electrode cycled in the operando cell without irradiation, showing the repartition of silicon (in red), LiF (in green), graphene sheets (in white) and polymeric part of the SEI (in blue). Panels (a), (b), and (c) correspond to different regions of the sample and represent three typical examples of the obtained images.*

X-ray photoelectron spectroscopy (XPS) experiments were also performed on both uncycled and cycled silicon electrodes (see Supporting Information, Figures S4-S5 and Table S1, for experimental details). Chemical composition and bonds already identified in literature (polymeric layer, LiF…)[27] were also measured without additional ones.

EIS measurements before and after cycling of the operando cell

Electrochemical impedance spectroscopy (EIS) measurements were performed before and after cycling (one cycle at C/40) of the *operando* cell. The impedance results are presented in Figure 5 and Table 1. Prior to cycling, the results show a low electrolyte resistance (Table 1), indicating good ionic conductivity within the cell. Additionally, no solid electrolyte interphase (SEI) formation was observed. The charge transfer resistance was also low (5 Ω, Table 1), and at that stage, we can only observe a blocking diffusion behavior, at lowest frequencies (vertical straight line). Post-cycling EIS analyses were conducted at the end of the delithiation phase. The electrolyte resistance remained similar to that measured before cycling. However, the impedance spectrum exhibited two distinct semicircles, corresponding to SEI formation and charge transfer processes, respectively (Figure 5). Furthermore, the diffusion phenomenon could now be modelled by a TLM element (DX), suggesting the presence of a tortuous diffusion process within the electrode material. The SEI resistance was relatively low

(22 Ω, Table 1), and the α_{SEI} coefficient of 0.75 indicated that the SEI layer formed was rather homogeneous across the surface of the negative electrode. The charge transfer resistance also remained low (32 Ω, Table 1). These last features suggest that the formed layer is primarily composed of conductive components so that the overall electrochemical kinetics remains efficient.

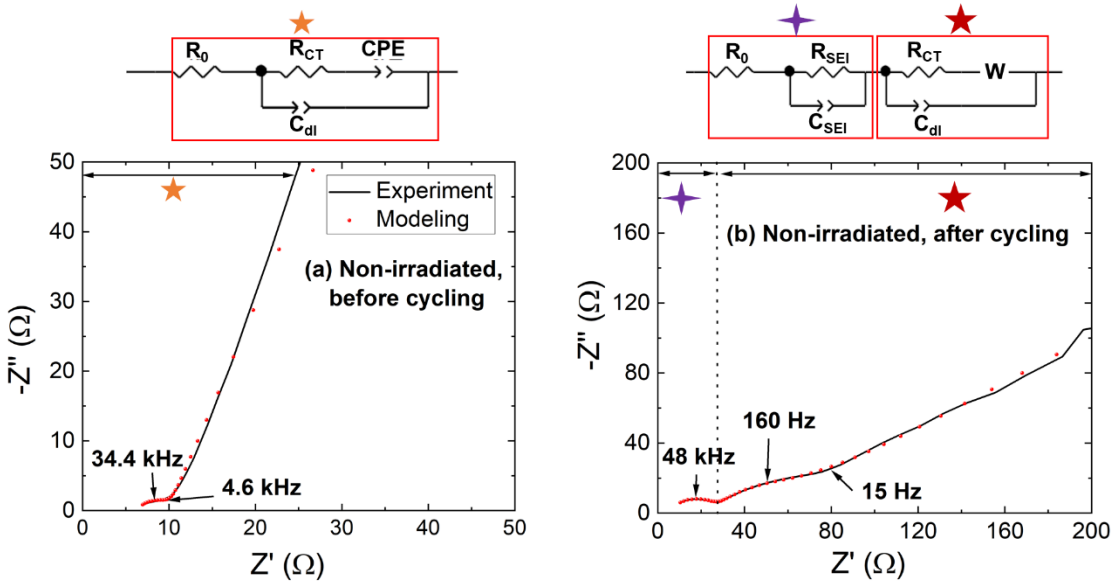

Figure 5. *Electrochemical impedance spectra before (a) and after (b) one cycle at C/40 of the operando cell. The electrical equivalent circuit (EEC) used for modeling is shown in the top panel. Some frequencies of interest are also indicated on the spectra (see arrows). The lines represent the experimental data, while the points correspond to the results of the modeling.*

Table 1. *Resistance (R), pseudo-capacitance (Q) and non-ideality factor (α) values obtained after modeling the electrochemical impedance spectra in Figures 4 and 8-9. A detailed discussion of the data obtained from the cell containing irradiated electrolyte is provided later in the manuscript.*

		R_0 (Ω)	R_{SEI} (Ω)	Q_{SEI} ($F.s^{\alpha}_{SEI}{}^{-1}$)	α_{SEI}	R_{CT} (Ω)	Q_{dl} ($F.s^{\alpha}_{dl}{}^{-1}$)	α_{dl}
Non-irradiated	Before cycling	6	/	/	/	5	$4 \cdot 10^{-5}$	0.70
	After cycling (one cycle at C/40)	5	22	$3 \cdot 10^{-6}$	0.75	32	$2 \cdot 10^{-4}$	0.70
Irradiated (5 kGy)	Before cycling	6	/	/	/	5	$7 \cdot 10^{-5}$	0.70
	After cycling (one cycle at	7	20	$1 \cdot 10^{-4}$	0.70	18	$3 \cdot 10^{-4}$	0.71

	C/40)							
Irradiated (10 kGy)	Before cycling	7	/	/	/	4	$1 \cdot 10^{-4}$	0.70
	After cycling (one cycle at C/40)	7	23	$1 \cdot 10^{-5}$	0.70	107	$7 \cdot 10^{-4}$	0.70

These detailed spectroscopic analyses confirm that the solid electrolyte interphase (SEI) formed in the *operando* cell is chemically comparable to that formed in full cells.[27, 33]

Impact of irradiation on electrochemical performance, gas production, and electrode evolution

The electrolyte was directly irradiated in the assembled cell to investigate the effects on cycling performance, gas evolution, and the composition of the SEI. To protect the electrodes, an aluminum plate approximately 5 cm wide was placed in front of the cell so that only a part of the electrolyte was exposed to the electron beam (Figure S1). Dosimetry experiments showed that a dose of 6 Gy (with a measurement uncertainty of about 10% and 1 Gy = 1 $J.kg^{-1}$) per pulse was delivered to the whole electrolyte. The electrolyte was irradiated at two distinct doses: 5 kGy and 10 kGy. The electron beam is pulsed, with individual electron pulses lasting 10 ns, and we operate at a repetition rate of 2 Hz to avoid any significant sample heating (see the Materials and Methods section). This means that during irradiation, the sample receives two 10 ns pulses per second, delivering a total dose of 12 Gy per second (with 6 Gy per pulse). To reach a total dose of 5 kGy, irradiation is performed for approximately 7 minutes, and this duration is doubled to achieve 10 kGy. Each irradiation is applied in a single session, resulting from the accumulation of multiple electron pulses received by the sample. These irradiation times are therefore much shorter than the electrochemical cycling times. For this reason, we chose to irradiate the cells first and then perform the cycling. Regarding dose rate, Blondeau *et al.* report that the electrolyte receives 18 kGy over 5 minutes of exposure in *operando* synchrotron experiments.[9] In our

experiments, the sample receives 3.6 kGy over 5 minutes. Therefore, the average dose rates in the two cases are of the same order of magnitude, differing by approximately a factor of five.

Impact of irradiation on cycling performance

After irradiation, charge/discharge cycling was performed, and the results for both 5 and 10 kGy doses are presented in Figure 6. Initially, the specific capacity of the cell with irradiated electrolytes (1856 and 2201 $mAh \cdot g^{-1}$) was significantly lower than that of the non-irradiated one (3357 $mAh \cdot g^{-1}$, Figure S6). This indicates that the effects of irradiation are immediate and can influence regions beyond the irradiation site, as the electrodes are located 1 cm away from the irradiated area. Furthermore, the discharge capacity evolves differently depending on the irradiation dose. At 5 kGy, despite the lower initial capacity, the cell recovers, and by the 20^{th} cycle, the capacity is comparable to that of the non-irradiated cell (Figure S6). In contrast, the cell exposed to 10 kGy experiences a continuous decline in capacity after the first cycle, ultimately ceasing to function after only four cycles (Figure S6). Another interesting observation from Figure S6 is that the capacity of the cell irradiated at low dose (5 kGy) remains notably more stable from cycle 7 through cycle 20, whereas the non-irradiated cell exhibits a continuous capacity decay -initially more pronounced up to cycle 5, then persisting at a slower rate during the subsequent cycles. We can propose a tentative explanation for this somewhat intriguing behaviour. The full capacity reached by the non-irradiated cell likely induces large volume changes, leading to extensive pulverization that severely limits long-term cycling stability. In contrast, the initially reduced capacity of the 5 kGy-irradiated cell considerably mitigates such structural changes (similar to limited-capacity protocols), thereby promoting a more stable response upon cycling. For the cell irradiated at 10 kGy, however, the irradiation likely generates a substantial amount of degradation products, possibly dissolved in the electrolyte, whose persistent and cumulative effects after the first cycle ultimately lead to the catastrophic failure observed. Clear voltage spikes observed during the charge process in cycles 2 and 3 (Figure 6b) further suggest electrode degradation induced by the migration of irradiated electrolyte components. These findings are consistent with earlier reports in which coin cells assembled with electrolytes pre-irradiated at 18 kGy failed to operate.[19]

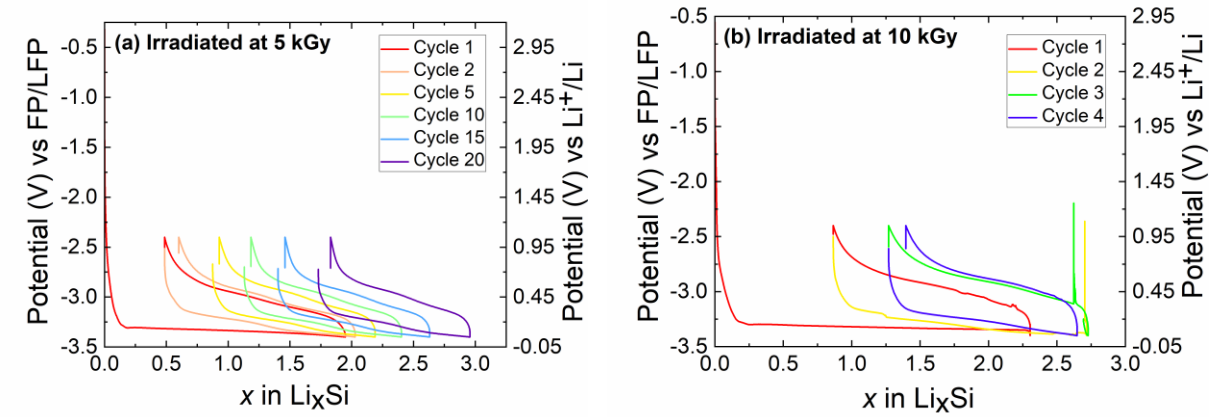

Figure 6. *Potential curves as a function of the number of lithium ions (x) exchanged between the two electrodes after electrolyte irradiation at a dose of 5 kGy (a) and 10 kGy (b).*

Impact of irradiation on gas production

The investigation on *operando* gas measurements were performed during the first cycle for the 5 kGy and 10 kGy irradiated electrolytes. The 1st cycle was operated at a C/40 rate (Figure 7). The initial measurement (for a State-of-Charge of 0) reflects the gases produced during the irradiation process. This initial gas production due to irradiation at relatively low doses (5 and 10 kGy) is low and negligible compared to the cumulative amounts of gas subsequently measured during cycling, although not strictly zero. Irradiation of the electrolyte resulted in the formation of CO_2, H_2, CO, and CH_4, as detected by gas-phase micro-chromatography - findings that are consistent with previous data.[40] The cell was purged between measurements to remove as much of the generated gas as possible. For the cell containing the electrolyte irradiated at 10 kGy, only the analyses during silicon lithiation could be carried out. This limitation is primarily due to the poor cycling stability of that cell.

During cycling with the irradiated electrolyte, H_2 is generated in the highest amount, followed by CO_2, which is produced at approximately half the quantity of H_2. CO is the third most abundant gas detected, while methane (CH_4) is present at levels roughly five times lower than CO. Notably, both CO and CH_4 were absent during cycling with the non-irradiated electrolyte (Figure 3). For H_2 and CO_2, the quantities produced exceed those observed with the non-irradiated electrolyte, and their levels increase with irradiation dose (Figure 7). The only exception is hydrogen, whose production remains relatively insensitive to the irradiation dose (Figure 7a). H_2 is predominantly generated during the lithiation phase, with significantly

lower production during delithiation. A similar, but more pronounced, behavior is observed for CO_2 (Figure 7b): its evolution rate decreases toward the end of lithiation and remains limited during delithiation. In contrast, CO generation occurs mainly during the early stages of lithiation (Figure 7c), as does CH_4 production, although CH_4 exhibits a slight resurgence during delithiation (Figure 7d).

By GC/MS, additional gases were detected during the cycling of cells containing irradiated electrolyte at different doses. The results of these analyses are presented in Figure S7. The same gases were produced at both doses, but the overall gas quantity increased after a 10 kGy irradiation compared to a 5 kGy irradiation, even though the cycling duration was shorter (solely the lithiation is presented due to cell failure). Gases such as C_2H_6, C_3H_8, CH_3CHO, and $HCOOCH_3$, which were not produced during the cycling of the *operando* cell with the non-irradiated electrolyte, were formed in the case of the irradiated electrolyte. It is also noteworthy that ester formation was observed in GC/MS experiments conducted on LP30 electrolyte contained in a stainless steel/Li cell cycled at 55°C.[39] In fact, these gases -except for CH_3CHO- had been previously identified during the irradiation of LP57 electrolyte (EC/EMC (3/7) + $LiPF_6$ 1 M) containing FEC.[40] These additional gases can be attributed to the irradiation of the electrolyte, which induces specific chemical reactions leading to their formation. Ortiz *et al.* also demonstrated that irradiation can generate minor compounds that are not produced during conventional electrochemical tests.[11-12, 18] The authors explained this observation by noting that ionizing radiation delivers a high dose of energy in a short time, thereby revealing the formation of species that are present only in trace amounts. Moreover, radiolysis tends to favor radical-radical reactions compared to electrochemical experiments. In the bulk electrolyte under irradiation, species arising from both reduction and oxidation pathways are generated simultaneously, in contrast to electrochemical experiments where these processes occur separately at each electrode.

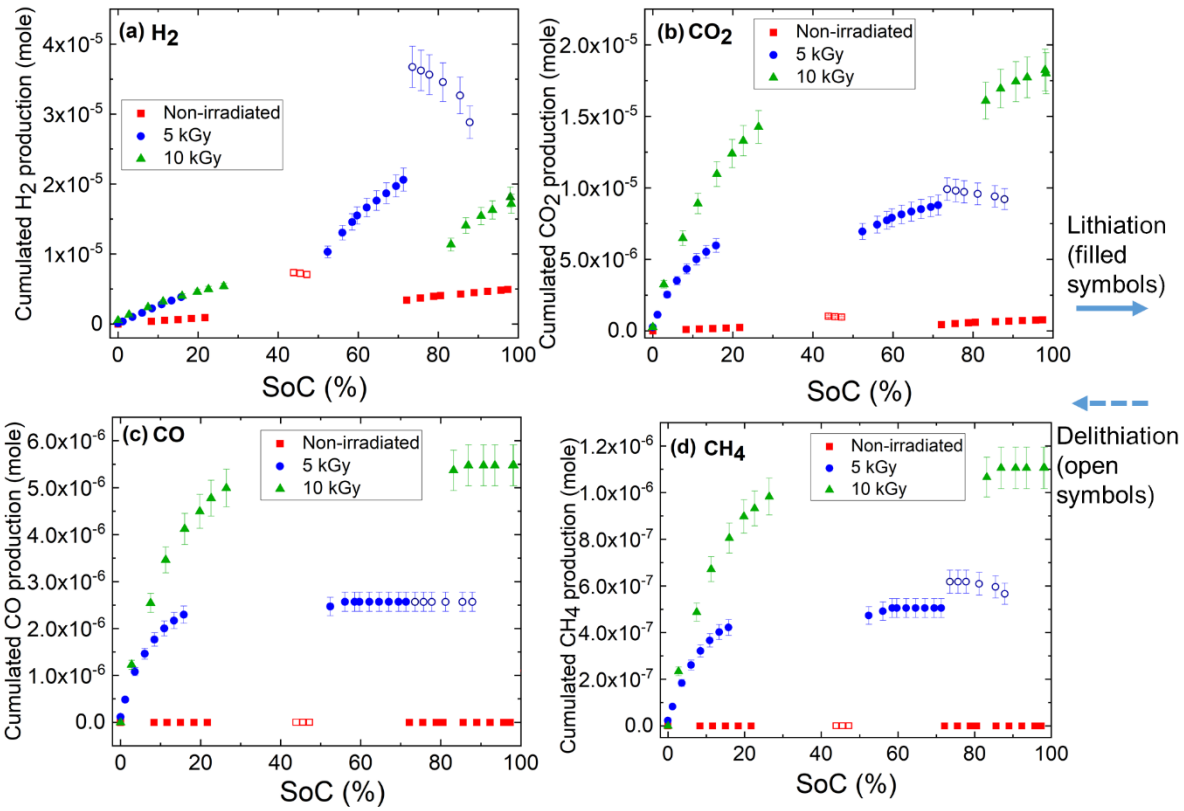

Figure 7. *Cumulative production of H_2 (a), CO_2 (b), CO (c), and CH_4 (d) during operando cell cycling after different irradiation doses of the electrolyte. Red squares represent the non-irradiated electrolyte, blue dots correspond to the electrolyte irradiated at 5 kGy, and green triangles indicate the electrolyte irradiated at 10 kGy. The first experimental data point represents the value obtained after electrolyte irradiation and before the start of cycling. Gas production is plotted as a function of the state of charge (SoC). Data obtained during lithiation are represented by filled symbols, whereas delithiation data are shown with open symbols. Lithiation corresponds to increasing SoC values (from left to right), while delithiation corresponds to decreasing SoC values (from right to left). For the electrolyte irradiated at 10 kGy, only lithiation could be performed.*

Irradiation leads to a significant increase in both the types and amounts of gases produced. Among the detected gases, H_2 is the only one whose generation shows limited sensitivity to the irradiation dose during the first cycle. Notably, its formation is linked to SEI development and the presence of trace water. Moreover, one possible explanation for its rise upon cycling time is the formation of HF under irradiation;[12, 18, 40] in the presence of the cell's glass, HF reacts to form SiF_4 and water molecules. This increase in water content naturally leads to enhanced molecular hydrogen formation over cycling time.

In addition to the gas-phase species generated by irradiation -which are purged before cycling-irradiation also forms liquid-phase species that remain in the system and continue reacting during cycling. In particular, methanol and methyl formate, although detected in the gas phase, are expected to be mainly dissolved in the liquid electrolyte under our experimental conditions; their presence in the liquid phase may lead to secondary reactions during cycling, which may contribute to additional gas formation, including CH_4 and CO, among others. Moreover, irradiating DEC/$LiPF_6$ solutions produces species such as $(F)_2(OCO_2C_2H_5)P{=}O$, leading to a delayed release of CO_2,[12] and similar reactions can be expected with DMC. Ionizing radiation also promotes the formation of PF_5, which reacts with traces of water to produce POF_3,[18] a compound known to catalyze carbonate decomposition and generate CO_2[41] Altogether, these processes likely contribute to the enhanced CO_2 (and other gases) production observed after irradiation and to its further increase with dose. Moreover, the reduction of ethylene carbonate yields CO, while that of DMC produces CH_4.[38, 42] However, in the presence of FEC, FEC preferentially decomposes, thereby preventing the formation of CO and CH_4.[36] The situation changes after irradiation. This raises questions about the quality of the SEI formed when the electrolyte has been exposed to irradiation. To address this issue, electrochemical impedance spectroscopy (EIS) measurements were performed.

EIS measurements after irradiation of the electrolyte of the operando cell

The electrochemical impedance spectra measured after irradiation of the electrolyte in the *operando* cell and prior to cycling are shown in Figure 8. The corresponding modeling results are provided in Table 1.

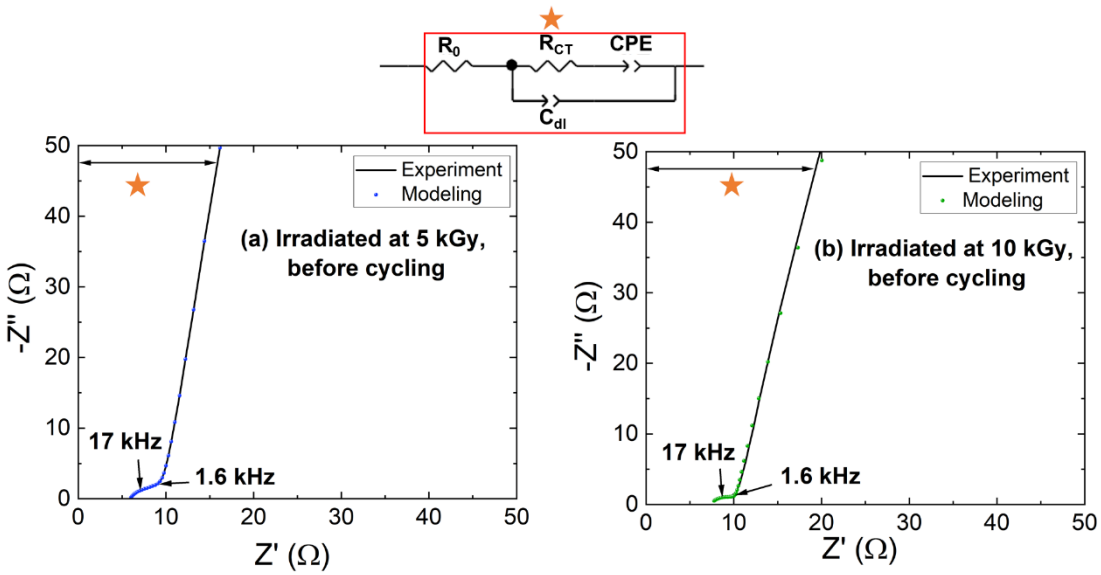

Figure 8. *Electrochemical impedance spectra obtained after irradiation of the operando cell electrolyte at 5 kGy (a) and 10 kGy (b). Measurements were performed prior to cell cycling. The equivalent electrical circuit (EEC) used for modeling is shown in the top panel. Some frequencies of interest are also indicated on the spectra (see arrows). The lines represent the experimental data, while the points correspond to the results of the modeling.*

A comparison of the pre-cycling results shows that the electrolyte resistance remains similar to that of the cell containing non-irradiated electrolyte, regardless of the irradiation dose (5 or 10 kGy, Table 1). No SEI formation was observed on the silicon surface after irradiation. Furthermore, the charge transfer resistance values were identical before and after irradiation of the electrolyte, as well as diffusion process, again limited here to blocking conditions. This suggests that, before cycling, the irradiation does not affect the electrical properties of the cell components.

These measurements were also recorded after cycling (one cycle at C/40, Figure 9). After cycling, the electrolyte resistance increased slightly in both irradiated cases -with a value of 7 Ω for electrolytes exposed to 5 and 10 kGy- compared to 5 Ω for the non-irradiated electrolyte (Table 1). Moreover, the results show that the SEI films formed in irradiated electrolytes exhibit similar resistance as that of the non-irradiated sample (20 Ω for the 5 kGy case, 23 Ω for 10 kGy, and 22 Ω for the non-irradiated electrolyte, Table 1). However, SEI layers formed with irradiated electrolytes are less homogeneous and more porous, as reflected by lower α_{SEI} values (0.70 for both 5 and 10 kGy irradiation) compared to 0.75 for the non-irradiated electrolyte, indicating a more uniform SEI in the latter case (Figure 5 and Table 1). Interestingly, after cycling, charge transfer resistance also decreased following irradiation at 5 kGy (18 Ω compared to 32 Ω for the non-irradiated electrolyte, Table 1). This could be

explained by the electrode surface accessibility thanks to the SEI patches and/or pores. In contrast, irradiation at 10 kGy led to a significant increase in charge transfer resistance (107 Ω, Table 1). Here, the electrochemical kinetics has been strongly impacted, which is consistent with the poor cyclability recorded (Figure 6). The diffusion processes, at lower frequencies, are also following the same trend, as after an irradiation at 10 kGy, a much more tortuous transport can be observed, which is detrimental for proper cycling performance. Moreover, the characteristic frequency of the SEI after irradiation and cycling shifted to 24 kHz (Figure 9), compared to 48 kHz for the non-irradiated electrolyte after cycling (Figure 5). This slight shift indicates that the SEI chemical composition has partially changed, leading most probably to different dielectric properties after irradiation (as conductivity is similar with equivalent R_{SEI} values, while C_{SEI} increases).

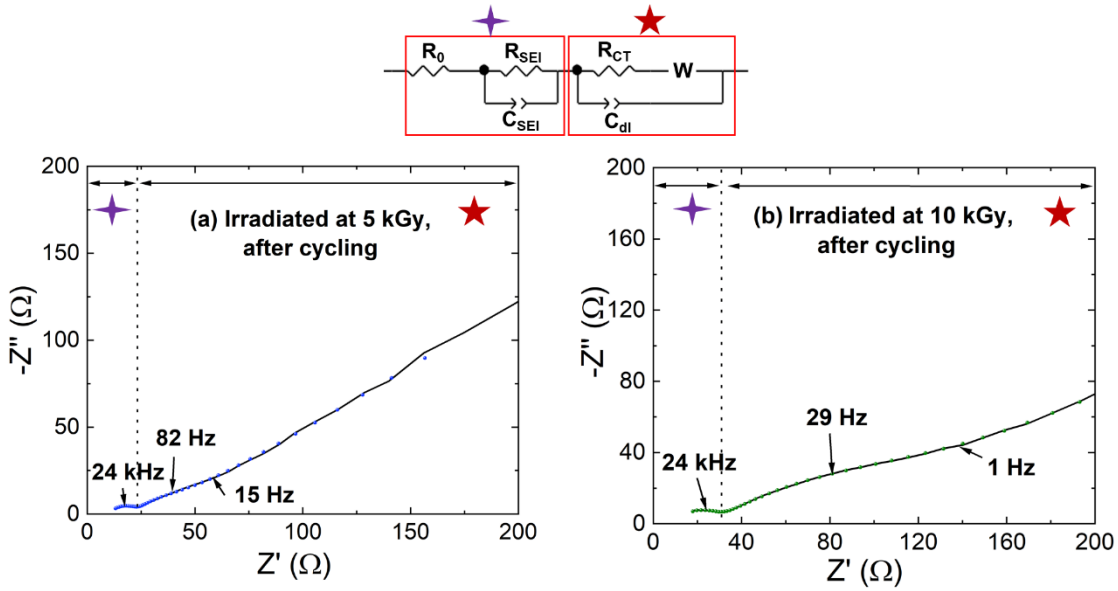

Figure 9. *Electrochemical impedance spectra obtained after irradiation of the operando cell electrolyte at 5 kGy (a) and 10 kGy (b). Measurements were performed after cell cycling (one cycle at C/40). The equivalent electrical circuit (EEC) used for modeling is shown in the top panel. Some frequencies of interest are also indicated on the spectra (see arrows). The lines represent the experimental data, while the points correspond to the results of the modeling.*

Therefore, the SEI layers formed after cycling with irradiated electrolytes appear to be slightly different in composition, inhomogeneous and/or porous, in contrast to the more uniform/denser SEI formed in the presence of non-irradiated electrolyte (see Table 1 and the corresponding Figures). This suggests an uneven distribution of the formed species and the presence of pores or non-uniform structures within the SEI layer. This inhomogeneous and/or porous SEI may promote the reduction of both ethylene carbonate and dimethyl carbonate,

leading to increased gas release, as observed in Figure 7. For instance, methyl radicals might be generated, which, upon reacting with hydrogen atoms from water reduction, can form CH_4.[38] The pores or irregularities in the SEI may also serve as favorable sites for gas bubble formation and retention. Moreover, irradiation generates liquid-phase degradation products, which can, in turn, lead to additional gas formation during cycling (see Figure S7). Lastly, the origin of the more porous SEI observed when only the electrolyte has been irradiated remains an open question. Irradiation can lead to the formation of solid degradation products (such as LiF), which may deposit non-uniformly on the electrode surface. These species are present during the initial SEI formation cycle and are likely to influence its structure and composition.

These observations highlight the complex mechanisms that may be at play during irradiation and cell cycling, potentially leading to unusual or unexpected reactions.

Evolution of the surface of the electrode after irradiation

Although the limited statistical significance of the STEM-EELS experiments warrants caution, several observations can still be made after a first cycle at C/40. First, after irradiation of the electrolyte at 5 kGy, the electrode does not appear to be fully charged (delithiated). The presence of an Li_xSi alloy is clearly identified (Figure 10) owing to the measurement of a plasmon peak at 15.0(2) eV in the low-energy loss spectrum, which suggests a $Li_{\approx 1}Si$ composition.[32] This alloy is less lithium-rich than the composition observed in *post-mortem* analyses after 100 cycles in Swagelok cells ($x \approx 1.5$),[33] but it aligns with the hypothesis that particle disconnection occurs at such compositions due to volume shrinkage. Interestingly, unlike previous observations,[33] the lithiated phase is not located in the inner part of the particles but instead surrounds a silicon core. This suggests that portions of the silicon material never underwent lithiation throughout cycling. Local increase of impedance due to a more inhomegeneous SEI as inferred from EIS measurements could explain this phenomenon, potentially contributing to both the electrode's capacity loss and its inability to achieve full delithiation (as indicated by the presence of the $Li_{\approx 1}Si$ alloy). Additionally, an organic SEI/binder layer (in blue) covered by an LiF-rich inorganic layer (in green) is observed, which is a typical situation (Figure 10).[33]

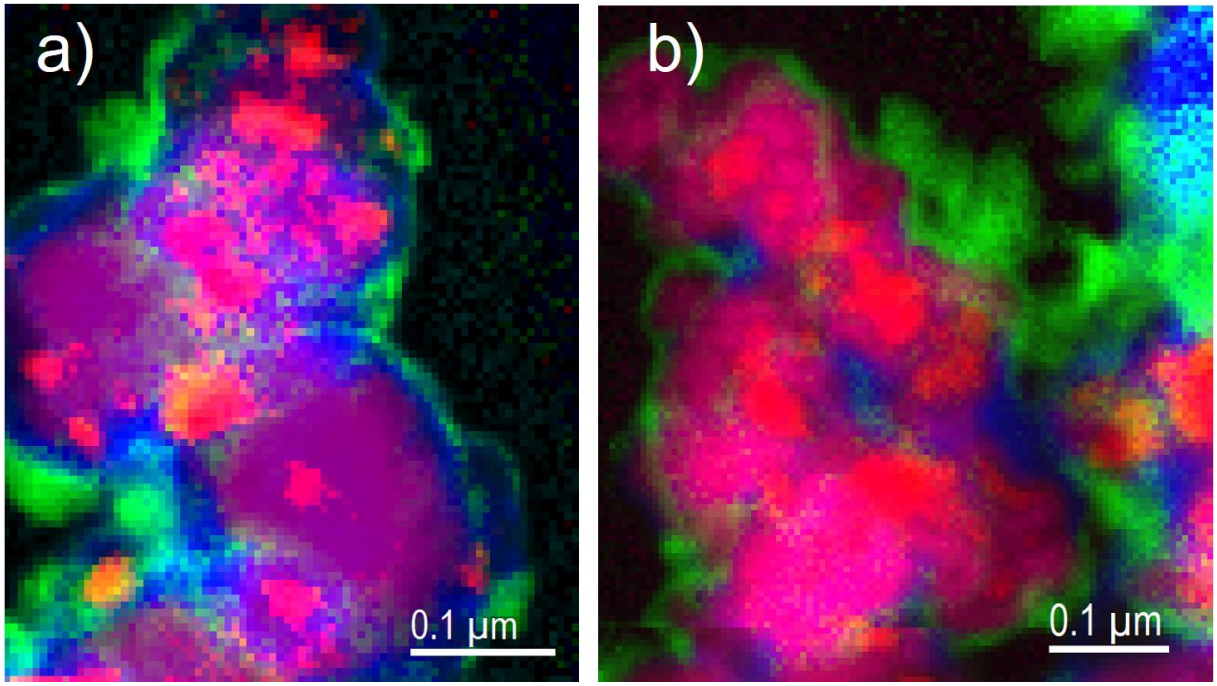

Figure 10. *Phase maps obtained from STEM-EELS experiments on an electrode cycled in the operando cell after a 5 kGy irradiation, showing the repartition of silicon (in red), $Li_{\approx 1}Si$ alloy (in purple), LiF (in green), graphene sheets (in white) and of the polymeric part of the SEI (in blue). Panels (a) and (b) correspond to different regions of the sample and represent three typical examples of the obtained images.*

For the 10 kGy irradiation, the delithiation process appears to be complete, as no Li_xSi alloy was detected in any of the analyzed aggregates. Notably, large polymeric patches were observed (Figure 11), aside of the silicon particles, with some reaching sizes of approximately 100 nm -significantly larger than the sub-50 nm structures observed in other samples (Figure 10, corresponding to the 5 kGy case). This suggests that a higher irradiation dose may promote an organic SEI formation and/or larger deposits coming from novel reactive species. Although statistics from microscopy experiments are usually considered limited, these results are consistent with a possible global compositional change of the SEI, as inferred from EIS measurements. These patches may, of course, form following substantial gas release, as evidenced by the gas-phase measurements.

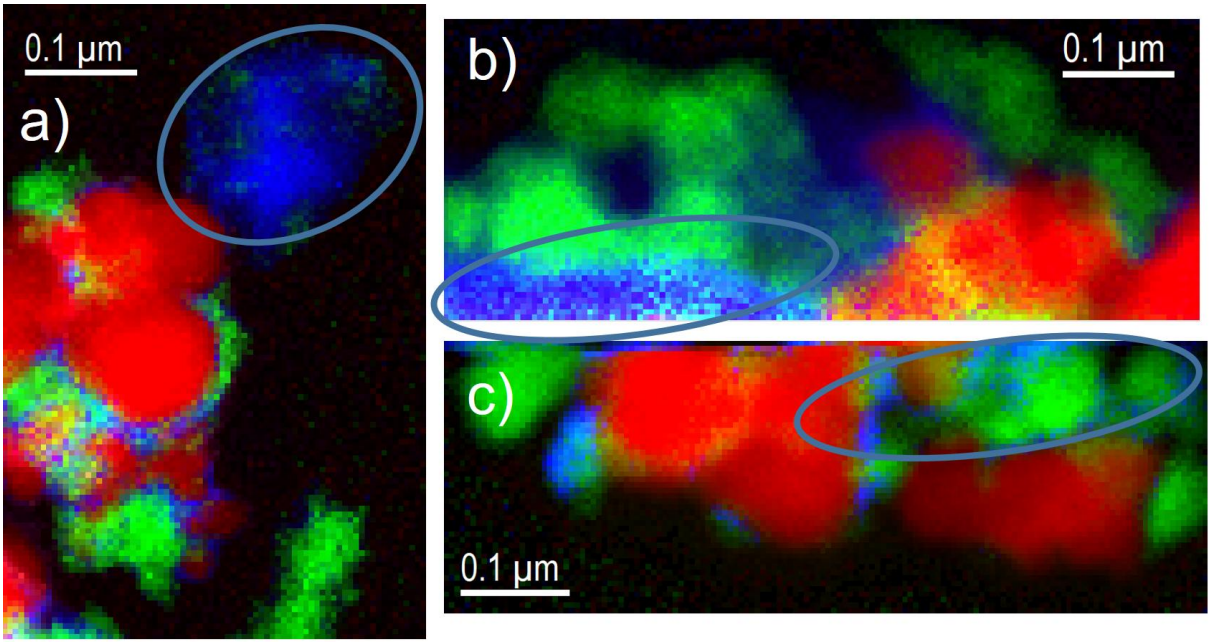

***Figure 11**. Phase maps obtained from STEM-EELS experiments on an electrode cycled in the operando cell after a 10 kGy irradiation, showing the repartition of silicon (in red), LiF (in green), graphene sheets (in white) and of the polymeric part of the SEI (in blue). Unusually large polymeric deposits are circled. Panels (a), (b), and (c) correspond to different regions of the sample and represent three typical examples of the obtained images.*

XPS data collected on silicon electrodes from *operando* cells in which the electrolyte was irradiated at 5 and 10 kGy, followed by one cycle at C/40, are consistent with the results obtained by STEM-EELS (see Figures S8-S9, Table S1 and the corresponding discussion). Although the XPS spectra measured after cycling exhibit many similarities, some differences attributable to irradiation are also evident. In particular, in the irradiated samples, the fluorine 1s spectrum exhibits a contribution at a binding energy similar to that of $LiPF_6$. In fact, the presence of electrolyte salt within the electrode after electrolyte irradiation is consistent with a non-uniform and porous SEI, which could retain $LiPF_6$ during rinsing (Figure S9).

Conclusion

This study presents a comprehensive investigation of the effects of ionizing radiation on lithium-ion battery components using a purpose-designed *operando* cell, which replicates synchrotron irradiation conditions while allowing precise monitoring of electrochemical, chemical, and post-mortem electrode evolution. By selectively irradiating the electrolyte at controlled doses (5 and 10 kGy), we revealed how even spatially localized radiation exposure can lead to system-wide consequences in lithium-ion cells. This study focuses on the response of a silicon electrode, which is well known to be highly sensitive to the composition of the electrolyte with which it is in contact. Consequently, the conclusions drawn here should not be directly extrapolated to Ni-rich positive electrodes or to standard *operando* synchrotron configurations. Although an equivalent in-depth investigation on a Ni-rich positive electrode is essential to accurately assess the impact of electrolyte irradiation on a complete system, these findings highlight the interconnected nature of electrochemical components and call into question the common assumption that irradiation only affects the directly exposed region.

Electrochemical testing showed that irradiation induced an immediate reduction in the specific capacity, with the extent of degradation strongly depending on the irradiation dose. At 10 kGy, the cell underwent rapid performance loss and failed after only a few cycles, whereas the 5 kGy-irradiated system demonstrated partial recovery. Indeed, the migration of radiolysis products from the irradiated electrolyte affect electrode stability and long-term function.

Gas-phase analyses revealed a marked increase in gas generation following irradiation, with H_2 and CO_2 being dominant. Importantly, additional gases such as CO, CH_4, C_2H_6, and CH_3CHO -absent in non-irradiated systems- were detected, indicating that irradiation triggers distinct degradation pathways. While most gases showed dose-dependent production, H_2 displayed only limited sensitivity to irradiation dose. This behavior likely stems from residual water content, which may increase with cycling time.

Electrochemical Impedance Spectroscopy experiments and *post-mortem* analysis of the electrode surfaces by STEM-EELS revealed significant structural changes in the SEI after irradiation of the electrolyte. In contrast to the more uniform and passivating SEI observed in non-irradiated cells, irradiated cells exhibited porous, inhomogeneous SEI layers. These morphologies facilitate further solvent reduction, enhance gas generation, and possibly impair lithium transport. After irradiation at 5 kGy, the electrode remained partially charged, in contrast to the complete discharge observed at 10 kGy. At this higher dose, polymeric surface

deposits were observed aside of silicon particles, indicating that electrolyte irradiation affects both the interfacial chemistry and the electrode's electrochemical behavior. In fact, the degradation products generated under irradiation lead to the formation of a more porous and less homogeneous SEI, which in turn enhances gas evolution during cycling and ultimately impairs the proper functioning of the cell.

Overall, this work provides critical insight into the complexity of radiation-induced degradation in lithium-ion batteries. It demonstrates that even localized irradiation can have far-reaching effects due to the coupling between electrolyte and electrode processes. These findings are highly relevant for the design and interpretation of synchrotron-based *operando* experiments, which must consider radiation artifacts to avoid misinterpreting ageing phenomena. More broadly, this study also opens perspectives for using radiation as a tool to accelerate ageing in controlled ways, helping to identify degradation mechanisms and to design more robust battery chemistries and architectures.

Associated Content

Supporting Information

Photograph of the *operando* cell; capacity curves; monitoring bubble formation; chromatogram measured after cycling; XPS spectra; capacity evolution as a function of the number of cycles; chromatograms measured after irradiation followed by cycling.

Acknowledgments

We thank the CEA's Focus Batteries program, as well as funding from the French National Research Agency (ANR ACETONE N° ANR-20-CE09-0010-01) for financial support. We would also like to thank the French EMIR&A network and Jorge Vieira for providing irradiation beam time at the ALIENOR platform. All transmission electron microscopy measurements were carried out with the Nant'Themis, part of IMN's characterization platform, PLASSMAT, Nantes, France. Dr Magali Gauthier is gratefully acknowledged for fruitful discussions and for help.

References

(1) Liu, D.; Shadike, Z.; Lin, R.; Qian, K.; Li, H.; Li, K.; Wang, S.; Yu, Q.; Liu, M.; Ganapathy, S. et al. Review of Recent Development of in Situ/Operando Characterization Techniques for Lithium Battery Research. *Adv. Mater.* **2019**, *31*, 1806620.

(2) Boebinger, M. G.; Lewis, J. A.; Sandoval, S. E.; McDowell, M. T. Understanding Transformations in Battery Materials Using in Situ and Operando Experiments: Progress and Outlook. *ACS Energy Lett.* **2020**, *5*, 335-345.

(3) Li, W.; Lutz, D. M.; Wang, L.; Takeuchi, K. J.; Marschilok, A. C.; Takeuchi, E. S. Peering into Batteries: Electrochemical Insight through in Situ and Operando Methods over Multiple Length Scales. *Joule* **2021**, *5*, 77-88.

(4) Cho, B.-K.; Jung, S.-Y.; Park, S.-J.; Hyun, J.-H.; Yu, S.-H. In Situ/Operando Imaging Techniques for Next-Generation Battery Analysis. *ACS Energy Lett.* **2024**, *9*, 4068-4092.

(5) Lou, S.; Sun, N.; Zhang, F.; Liu, Q.; Wang, J. Tracking Battery Dynamics by Operando Synchrotron X-Ray Imaging: Operation from Liquid Electrolytes to Solid-State Electrolytes. *Acc. Mater. Res.* **2021**, *2*, 1177-1189.

(6) Black, A. P.; Sorrentino, A.; Fauth, F.; Yousef, I.; Simonelli, L.; Frontera, C.; Ponrouch, A.; Tonti, D.; Palacín, M. R. Synchrotron Radiation Based Operando Characterization of Battery Materials. *Chem. Sci.* **2023**, *14*, 1641-1665.

(7) Fan, Y.; Wang, X.; Bo, G.; Xu, X.; See, K. W.; Johannessen, B.; Pang, W. K. Operando Synchrotron X-Ray Absorption Spectroscopy: A Key Tool for Cathode Material Studies in Next-Generation Batteries. *Adv. Sci.* **2025**, 2414480.

(8) Bras, W.; Myles, D. A. A.; Felici, R. When X-Rays Alter the Course of Your Experiments. *J. Phys.: Condensed Matter* **2021**, *33*, 423002.

(9) Blondeau, L.; Surblé, S.; Foy, E.; Khodja, H.; Belin, S.; Gauthier, M. Are Operando Measurements of Rechargeable Batteries Always Reliable? An Example of Beam Effect with a Mg Battery. *Anal. Chem.* **2022**, *94*, 9683-9689.

(10) Christensen, C. K.; Karlsen, M. A.; Drejer, A.; Andersen, B. P.; Jakobsen, C. L.; Johansen, M.; Sørensen, D. R.; Kantor, I.; Jørgensen, M. R. V.; Ravnsbæk, D. B. Beam Damage in Operando X-Ray Diffraction Studies of Li-Ion Batteries. *Journal of synchrotron radiation* **2023**, *30*, 561-570.

(11) Ortiz, D.; Steinmetz, V.; Durand, D.; Legand, S.; Dauvois, V.; Maître, P.; Le Caër, S. Radiolysis as a Solution for Accelerated Ageing Studies of Electrolytes in Lithium-Ion Batteries. *Nature Comm.* **2015**, *6*, 6950.

(12) Ortiz, D.; Jimenez Gordon, I.; Baltaze, J.-P.; Hernandez-Alba, O.; Legand, S.; Dauvois, V.; Si Larbi, G.; Schmidhammer, U.; Marignier, J. L.; Martin, J.-F. et al. Electrolytes Ageing in Lithium-Ion Batteries: A Mechanistic Study from Picosecond to Long Timescales. *ChemSusChem* **2015**, *8*, 3605-3616.

(13) Li, M.; Liu, W.; Luo, D.; Chen, Z.; Amine, K.; Lu, J. Evidence of Morphological Change in Sulfur Cathodes Upon Irradiation by Synchrotron X-Rays. *ACS Energy Lett.* **2022**, *7*, 577-582.

(14) Jousseaume, T.; Colin, J.-F.; Chandesris, M.; Lyonnard, S.; Tardif, S. How Beam Damage Can Skew Synchrotron Operando Studies of Batteries. *ACS Energy Lett.* **2023**, *8*, 3323-3329.

(15) Black, A. P.; Escudero, C.; Fauth, F.; Fehse, M.; Agostini, G.; Reynaud, M.; Houdeville, R. G.; Chatzogiannakis, D.; Orive, J.; Ramo-Irurre, A. et al. Beam Effects in Synchrotron Radiation Operando Characterization of Battery Materials: X-Ray Diffraction and Absorption Study of $LiNi_{0.33}Mn_{0.33}Co_{0.33}O_2$ and $LiFePO_4$ Electrodes. *Chem. Mater.* **2024**, *36*, 5596-5610.

(16) Borkiewicz, O. J.; Wiaderek, K. M.; Chupas, P. J.; Chapman, K. W. Best Practices for Operando Battery Experiments: Influences of X-Ray Experiment Design on Observed Electrochemical Reactivity. *J. Phys. Chem. Lett.* **2015**, *6*, 2081-2085.

(17) Lawrence Bright, E.; Giacobbe, C.; Wright, J. P. Beam Heating from a Fourth-Generation Synchrotron Source. *Journal of synchrotron radiation* **2021**, *28*, 1377-1385.
(18) Ortiz, D.; Jimenez Gordon, I.; Legand, S.; Dauvois, V.; Baltaze, J.-P.; Marignier, J. L.; Martin, J.-F.; Belloni, J.; Mostafavi, M.; Le Caër, S. Role of PF_6^- in the Radiolytical and Electrochemical Degradation of Propylene Carbonate Solutions. *J. Power Sources* **2016**, *326*, 285-295.
(19) Souid, Y.; Herlin-Boime, N.; Franger, S.; Le Caër, S. Radiation Chemistry as a Tool to Accelerate and Predict Calendar Ageing in Lithium-Ion Batteries. *J. Electrochem. Soc.* **2024**, *171*, 090527.
(20) Paillot, M.; Wong, A.; Denisov, S. A.; Soudan, P.; Poizot, P.; Montigny, B.; Mostafavi, M.; Gauthier, M.; Le Caër, S. Predicting Degradation Mechanisms in Lithium Bistriflimide "Water-in-Salt" Electrolytes for Aqueous Batteries. *ChemSusChem* **2023**, *16*, e202300692.
(21) Puget, M.; Shcherbakov, V.; Denisov, S.; Moreau, P.; Dognon, J.-P.; Mostafavi, M.; Le Caër, S. Reaction Mechanisms of the Degradation of Fluoroethylene Carbonate, an Additive of Lithium-Ion Batteries, Unraveled by Radiation Chemistry. *Chem. Eur. J.* **2021**, *27*, 8185-8194.
(22) Souid, Y.; Puget, M.; Ortiz, D.; Piveteau, L.; Denisov, S.; Herlin-Boime, N.; Mostafavi, M.; Dognon, J.-P.; Le Caër, S. Radiation Chemistry Reveals the Reaction Mechanisms Involved in the Reduction of Vinylene Carbonate in the Solid Electrolyte Interphase of Lithium-Ion Batteries. *ChemSusChem* **2025**, *18*, e202402091.
(23) Spinks, J. W. T.; Woods, R. J., *An Introduction to Radiation Chemistry*, 3rd ed.; Wiley-Interscience Publication: New York, USA, 1990, p 243-313.
(24) Attwood, D.; Sakdinawat, A., *X-Rays and Extreme Ultraviolet Radiation: Principles and Applications*, 2016.
(25) Als-Nielsen, J.; McMorrow, D., *Elements of Modern X-Ray Physics*, 2011.
(26) Oumellal, Y.; Delpuech, N.; Mazouzi, D.; Dupré, N.; Gaubicher, J.; Moreau, P.; Soudan, P.; Lestriez, B.; Guyomard, D. The Failure Mechanism of Nano-Sized Si-Based Negative Electrodes for Lithium Ion Batteries. *J. Mater. Chem.* **2011**, *21*, 6201-6208.
(27) Dupre, N.; Moreau, P.; De Vito, E.; Quazuguel, L.; Boniface, M.; Bordes, A.; Rudisch, C.; Bayle-Guillemaud, P.; Guyomard, D. Multiprobe Study of the Solid Electrolyte Interphase on Silicon-Based Electrodes in Full-Cell Configuration. *Chem. Mater.* **2016**, *28*, 2557-2572.
(28) Kana, N.; Olivier-Archambaud, S.; Devic, T.; Lestriez, B. Tannic Acid as a Binder and Electronic Conductor Precursor in Silicon Electrodes for Li-Ion Batteries. *Electrochem. Comm.* **2023**, *151*, 107495.
(29) Xu, C.; Lindgren, F.; Philippe, B.; Gorgoi, M.; Björefors, F.; Edström, K.; Gustafsson, T. Improved Performance of the Silicon Anode for Li-Ion Batteries: Understanding the Surface Modification Mechanism of Fluoroethylene Carbonate as an Effective Electrolyte Additive. *Chem. Mater.* **2015**, *27*, 2591-2599.
(30) Schiele, A.; Breitung, B.; Hatsukade, T.; Berkes, B. B.; Hartmann, P.; Janek, J.; Brezesinski, T. The Critical Role of Fluoroethylene Carbonate in the Gassing of Silicon Anodes for Lithium-Ion Batteries. *ACS Energy Lett.* **2017**, *2*, 2228-2233.
(31) Vanpeene, V.; Stamati, O.; Guilloud, C.; Tucoulou, R.; Holliger, B.; Chandesris, M.; Lyonnard, S.; Villanova, J. Comparative Study of the Quantitative Analysis of Battery Materials with X-Ray Nano-Tomography: From Ex Situ toward Operando Measurements. *ACS Nano* **2025**, *19*, 9994-10012.
(32) Boniface, M.; Quazuguel, L.; Danet, J.; Guyomard, D.; Moreau, P.; Bayle-Guillemaud, P. Nanoscale Chemical Evolution of Silicon Negative Electrodes Characterized by Low-Loss Stem-Eels. *Nano Lett.* **2016**, *16*, 7381-7388.
(33) Xiong, J.; Dupré, N.; Moreau, P.; Lestriez, B. From the Direct Observation of a PAA-Based Binder Using STEM-VEELS to the Ageing Mechanism of Silicon/Graphite Anode

with High Areal Capacity Cycled in an FEC-Rich and EC-Free Electrolyte. *Adv. Energy Mater.* **2022**, *12*, 2103348.
(34) Rowden, B.; Garcia-Araez, N. A Review of Gas Evolution in Lithium Ion Batteries. *Energy Rep.* **2020**, *6*, 10-18.
(35) Schiele, A.; Breitung, B.; Mazilkin, A.; Schweidler, S.; Janek, J.; Gumbel, S.; Fleischmann, S.; Burakowska-Meise, E.; Sommer, H.; Brezesinski, T. Silicon Nanoparticles with a Polymer-Derived Carbon Shell for Improved Lithium-Ion Batteries: Investigation into Volume Expansion, Gas Evolution, and Particle Fracture. *ACS Omega* **2018**, *3*, 16706-16713.
(36) Jung, R.; Metzger, M.; Haering, D.; Solchenbach, S.; Marino, C.; Tsiouvaras, N.; Stinner, C.; Gasteiger, H. A. Consumption of Fluoroethylene Carbonate (FEC) on Si-C Composite Electrodes for Li-Ion Batteries. *J. Electrochem. Soc.* **2016**, *163*, A1705-A1716.
(37) Bernhard, R.; Metzger, M.; Gasteiger, H. A. Gas Evolution at Graphite Anodes Depending on Electrolyte Water Content and SEI Quality Studied by on-Line Electrochemical Mass Spectrometry. *J. Electrochem. Soc.* **2015**, *162*, A1984-A1989.
(38) Salomez, B.; Grugeon, S.; Armand, M.; Tran-Van, P.; Laruelle, S. Review—Gassing Mechanisms in Lithium-Ion Battery. *J. Electrochem. Soc.* **2023**, *170*, 050537.
(39) Gachot, G.; Ribière, P.; Mathiron, D.; Grugeon, S.; Armand, M.; Leriche, J.-B.; Pilard, S.; Laruelle, S. Gas Chromatography/Mass Spectrometry as a Suitable Tool for the Li-Ion Battery Electrolyte Degradation Mechanisms Study. *Anal. Chem.* **2011**, *83*, 478-485.
(40) Levieux-Souid, Y.; Martin, J.-F.; Moreau, P.; Herlin-Boime, N.; Le Caër, S. Radiolysis of Electrolytes in Batteries: A Quick and Efficient Screening Process for the Selection of Electrolyte-Additive Formulations. *Small Methods* **2022**, *6*, 2200712.
(41) Campion, C. L.; Li, W. T.; Lucht, B. L. Thermal Decomposition of $LiPF_6$-Based Electrolytes for Lithium-Ion Batteries. *J. Electrochem. Soc.* **2005**, *152*, A2327-A2334.
(42) Liu, P.; Yang, L.; Xiao, B.; Wang, H.; Li, L.; Ye, S.; Li, Y.; Ren, X.; Ouyang, X.; Hu, J. et al. Revealing Lithium Battery Gas Generation for Safer Practical Applications. *Adv. Funct. Mater.* **2022**, *32*, 2208586.

TOC

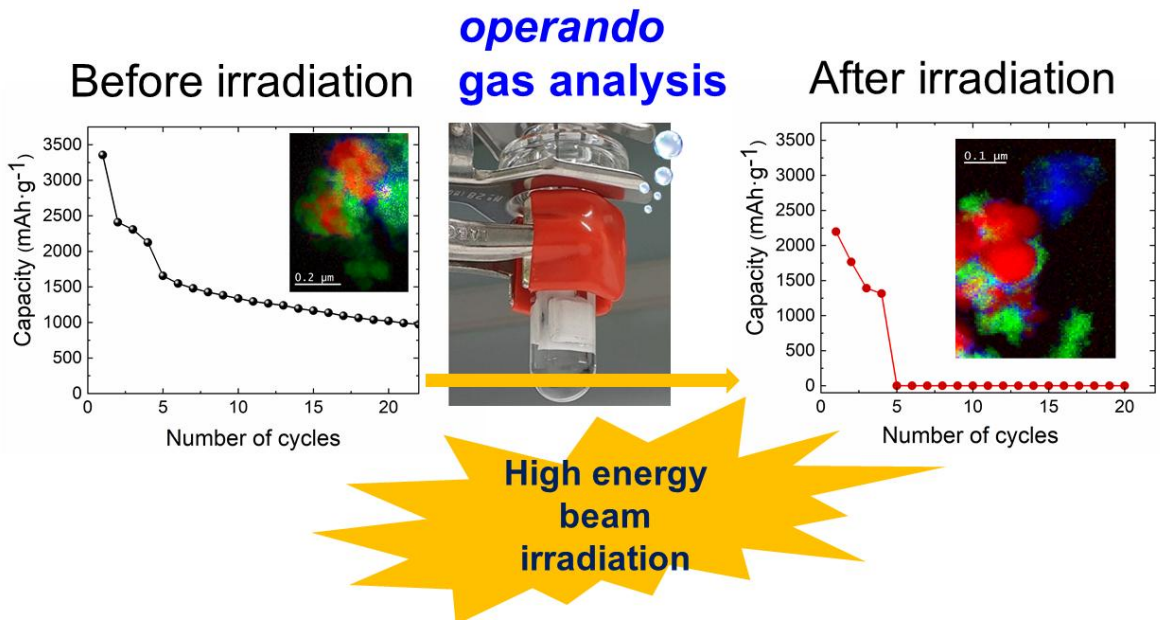
Before irradiation
operando
gas analysis
After irradiation
Capacity (mAh·g-1)
Number of cycles
0.2 μm
0.1 μm
High energy
beam
irradiation